PHYSICAL REVIEW E **93**, 063302 (2016)

Entropic lattice Boltzmann model for gas dynamics: Theory, boundary conditions, and implementation

N. Frapolli,[*] S. S. Chikatamarla,[†] and I. V. Karlin[‡]

Department of Mechanical and Processes Engineering, ETH Zurich, CH-8092 Zurich, Switzerland

(Received 9 March 2016; published 7 June 2016)

We present in detail the recently introduced entropic lattice Boltzmann model for compressible flows [N. Frapolli *et al.*, Phys. Rev. E **92**, 061301(R) (2015)]. The model is capable of simulating a wide range of laminar and turbulent flows, from thermal and weakly compressible flows to transonic and supersonic flows. The theory behind the construction of the model is laid out and its thermohydrodynamic limit is discussed. Based on this theory and the hydrodynamic limit thereof, we also construct the boundary conditions necessary for the simulation of solid walls. We present the inlet and outlet boundary conditions as well as no-slip and free-slip boundary conditions. Details necessary for the implementation of the compressible lattice Boltzmann model are also reported. Finally, simulations of compressible flows are presented, including two-dimensional supersonic and transonic flows around a diamond and a NACA airfoil, the simulation of the Schardin problem, and the three-dimensional simulation of the supersonic flow around a conical geometry.

DOI: 10.1103/PhysRevE.93.063302

I. INTRODUCTION

Understanding the nature of compressible flows is crucial in many science and technology applications, ranging from magnetohydrodynamics and astrophysics to high-speed aerodynamics and turbomachinery, to mention a few. Despite their widespread applications, predicting the behavior of compressible flows remains a challenge. Particularly challenging is the interaction of shock waves, appearing in supersonic flow regions, with turbulent flows. Numerical methods for high-speed flows have been specialized into two main classes, one capable of dealing with smooth flows and the other with shocks, each with different properties. Standard discretization used for smooth flows can cause potentially dangerous Gibbs oscillations, leading to unstable schemes in the presence of shocks, whereas typical methods used to regularize shock calculations exhibit excessive numerical viscosity [1]. Therefore, the main approaches to high-speed compressible flows are hybrid schemes, which typically combine higher-order methods with weighted essentially nonoscillatory schemes (WENO) through shock sensors, which determines which scheme should be used. A current alternative to the latter are nonlinear artificial viscosity methods [1]. However, both approaches are characterized by complicated algorithms that can also depend on the setup under consideration. This precludes the development of efficient, high-fidelity, robust direct numerical simulation solvers that can seamlessly treat any type of compressible turbulent flow (subsonic, transonic, and supersonic).

Recently, the lattice Boltzmann method (LBM) has gained attention as an alternative method for the study of complex flows including turbulence, microscale flows, porous media, multiphase flows, relativistic hydrodynamic, soft glasses, and beyond [2,3]. The simplest LBM solves a set of discrete kinetic equations for the populations $f_i(\boldsymbol{x},t)$, designed to reproduce, in the hydrodynamic limit, the desired equations of fluid dynamics. Each population is associated with a discrete velocity $\boldsymbol{v}_i$ that fits into a regular spatial lattice with nodes $\boldsymbol{x}$ at time t. This formulation can be realized by a highly efficient stream-along-links-and-equilibrate-at-nodes algorithm, which proves to be very convenient for both computational efficiency and numerical accuracy.

Historically, the LBM was hindered by two main issues: the inability to reach high Reynolds numbers in the underresolved regime because of numerical instabilities [4] and the lack of Galilean invariance and accuracy of standard lattices [5]. The first issue was tackled with different approaches. These include the multiple-relaxation-time approach in order to relax different moments with different relaxation times [4,6–8]. The entropic LBM (ELBM) for incompressible flows [9–12] disentangled the LBM from the low-Reynolds-number regime by restoring the second law of thermodynamics (Boltzmann's H theorem). The regularized approach curtails the development of nonhydrodynamic modes by quenching them to equilibrium [13,14].

A robust extension for thermal and compressible flows, together with a compliant H theorem for guaranteeing stability of the simulations, was presented by the entropic theory of admissible higher-order lattices [15,16]. The entropic higher-order lattices had already been tested for turbulent flows simulations in [17], while more recently the same was applied to quasicompressible thermal flows in [18].

At the same time, a number of suggestions for the simulation of thermal and compressible flows were proposed in the literature, including the use of correction terms [19]; the use of two populations, one for mass and momentum and the other for the thermal energy [20] or total energy [21,22]; or the use of lattices with an increased number of velocities [23–28]. However, these suggestions were limited in application range: The correction terms introduced uncontrolled numerical dissipation, while the two-population approach is limited to the incompressible limit. The above multispeed lattices were quite limited in applications. Moreover, development of multispeed models was hindered due to the lack of appropriate wall boundary conditions. In [18] many of the requirements for the simulation of thermal quasicompressible flows (Ma $\lesssim 0.2$)

---

[*] frapolli@lav.mavt.ethz.ch

[†] chikatamarla@lav.mavt.ethz.ch

[‡] karlin@lav.mavt.ethz.ch

were met: No correction terms were needed, the model was not limited to the incompressible limit, and the entropy supporting the lattice proved to be stable also for turbulence. Furthermore, wall boundary conditions for multispeed lattices were also presented.

In a recent Rapid Communication [29] we extended the entropic LBM to the simulation of high-speed compressible flows, where the three key ingredients for such an extension were laid out, namely, admissible higher-order lattices, exact entropic equilibrium, and the entropic estimate. In the present paper we provide a detailed derivation of the model of [29] and of the boundary conditions, as well as further details on the implementation. Moreover, we present extensive benchmarking of the model. We start by presenting a set of lattices that needs to be employed to simulate compressible flows in Sec. II A. We then proceed by detailing the exact entropic equilibrium in Sec. II B. Next, the thermohydrodynamic limit is derived in Sec. II D. Details on the entropy estimate that is used as a built-in subgrid model and as a stabilizer for shocks are given in Sec. II E. In Sec. II F details on the implementation and realization of the model are provided. The theoretical part of the paper concludes with the presentation of the boundary conditions, in Sec. II G, for inlet, outlet, and wall boundary conditions. In particular, the differences between no-slip and free-slip boundary conditions with fixed temperature and adiabatic conditions are discussed. The model is validated by means of different two-dimensional setups and a three-dimensional setup in Sec. III. We summarize in Sec. IV.

II. ENTROPIC LATTICE BOLTZMANN MODEL FOR COMPRESSIBLE FLOWS

The starting point of the compressible lattice Boltzmann model is the conventional single-relaxation-time lattice Bhatnagar-Gross-Krook (LBGK) kinetic equation

$$f_i(\boldsymbol{x}+\boldsymbol{v}_i,t+1)-f_i(\boldsymbol{x},t)=2\beta(f_i^{\mathrm{eq}}-f_i). \qquad (1)$$

Here β is the relaxation parameter related to the viscosity and the thermal conductivity and f_i^{eq} is the local equilibrium that satisfies the conservation laws of mass ρ, momentum $\rho\boldsymbol{u}$, and translational energy E_{tr},

$$\{\rho,\rho\boldsymbol{u},2\rho E_{\mathrm{tr}}\}=\sum_{i=1}^{n}\{1,\boldsymbol{v}_i,v_i^2\}f_i^{\mathrm{eq}}(\rho,\boldsymbol{u},T), \qquad (2)$$

with the translational energy defined as

$$2\rho E_{\mathrm{tr}}=2C_v^{\mathrm{tr}}\rho T+\rho\boldsymbol{u}^2, \qquad (3)$$

where $C_v^{\mathrm{tr}}=D/2$ is the specific heat of an ideal gas at constant volume in D dimensions.

In the following, two key steps are employed to achieve the compressible entropic lattice Boltzmann model. First, a proper choice for the discrete velocities $\boldsymbol{v}_i$ will be made in Sec. II A. Second, evaluation of the equilibrium f_i^{eq} for high Mach numbers will be described in Sec. II B.

A. Lattices for the compressible ELBM

Using the standard nomenclature D2Qn for the lattices with n speeds in $D=2$ space dimension (D3Qn in $D=3$ space dimension), the hierarchy of lattices described in [15,30] is constructed as the tensor products of D copies of one-dimensional velocity sets V_k. For incompressible models, the standard lattice D1Q3, composed of the discrete velocity set $V_3=\{0;\pm1\}$, can be used. Once we move into the domain of thermal simulations, the quasicompressible flow can be simulated using the D1Q5 lattice (or D2Q5^2 and D3Q5^3 in two and three dimensions, respectively), with the velocity set $V_5=\{0;\pm1;\pm3\}$ (see [18]). For the case of fully compressible flows, the number of velocities needs to be increased further, depending on the Mach number to be reached in the simulations, and also on the required temperature range. Below, the criterion for the choice of number of lattice velocities is explained in more detail.

In order to select the length of the links associated with each population, it was shown in [15] that an entropic derivation should be employed. For the case of the thermal model with five velocities in one dimension (1D), for example, the admissible lattice is the one with velocities $v_i\in V_5=\{0;\pm1;\pm3\}$ (the obvious choice of $V_5=\{0;\pm1;\pm2\}$ is discarded due to the nonexistence of a supporting entropy function). Here we propose to extend further the lattice size to seven speeds in one dimension, the shortest of which is $V_7=\{0;\pm1;\pm2;\pm3\}$. In order to evaluate the accuracy of each lattice, in Fig. 1 we compare the aforementioned five V_5 and seven V_7 speed

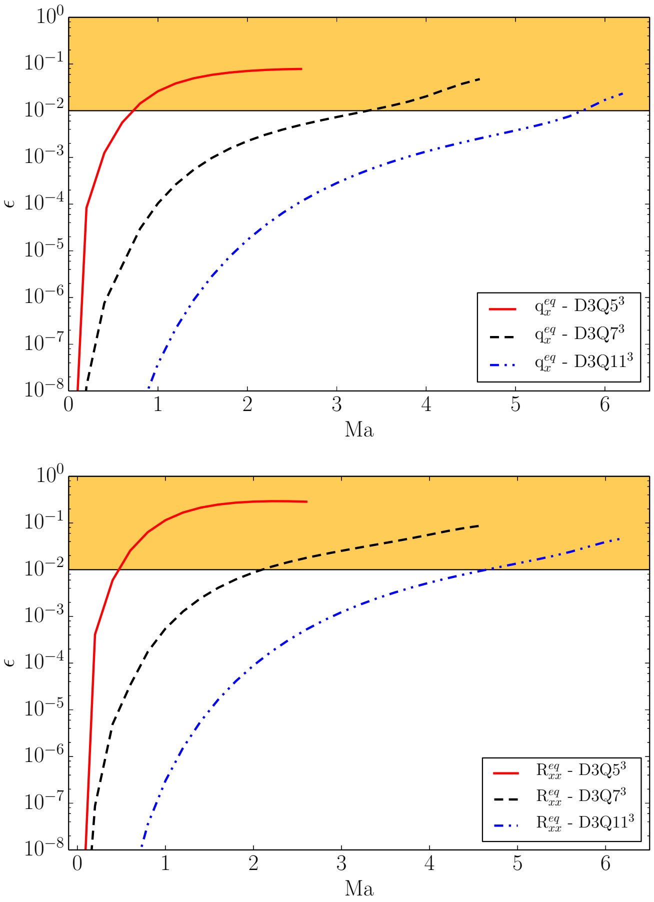

FIG. 1. Deviation of the x component of the lattice Boltzmann equilibrium energy flux q_x^{eq} (top) and flux of energy flux R_{xx}^{eq} (bottom) from the Maxwell-Boltzmann values computed at reference lattice temperature and varying Mach number.

lattices for the errors in evaluation of the equilibrium heat flux

$$q_\alpha^{\mathrm{eq}} = \sum_{i=1}^{n} f_i^{\mathrm{eq}} v_i^2 v_{i,\alpha} \tag{4}$$

and equilibrium contracted fourth-order moment

$$R_{\alpha\beta}^{\mathrm{eq}} = \sum_{i=1}^{n} f_i^{\mathrm{eq}} v_i^2 v_{i,\alpha\beta} \tag{5}$$

when compared to their Maxwell-Boltzmann (infinite set of velocities) counterparts at various Mach numbers. Together, for completeness, the errors of the D3Q11 velocities lattice $V_{11} = \{0; \pm1; \pm3; \pm4; \pm5\}$ are also shown. All errors are evaluated at reference temperature T_0, which is lattice dependent.

It is important to notice that the aforementioned moments need to be recovered accurately by the kinetic model in order to recover the correct thermohydrodynamic limit, as shown in Sec. II D. From Fig. 1 one can notice that the errors in the moments are small until Mach number of about $\mathrm{Ma} \leqslant 2$ for the lattice with seven velocities. This lattice has all the characteristics required to run compressible flow simulations, such as accuracy at relatively high Mach numbers, a supported entropy function, and a high-temperature range (detailed later), for which positivity of the populations is guaranteed. It is important to notice that if one needs to increase the Mach number, with the entropic lattice Boltzmann model it is just required to increase the number of lattice velocities. For example, from Fig. 1 it is possible to observe that with the 11-speed lattice it is possible to simulate flows where the Mach number can reach values until $\mathrm{Ma} \leqslant 4$, thus further validating the hierarchy of lattices proposed in [15,16].

B. Equilibrium for the compressible ELBM

The second key innovation of the compressible ELBM model is the form and evaluation of the equilibrium. Three mainstream approaches were followed in the literature to derive the equilibrium for the lattice Boltzmann equation. The first and most popular is the top-down approach [3], essentially based on writing the equilibrium in the form of a polynomial and then tuning the coefficients to recover the (Fourier-)Navier-Stokes equations [23,31] as the limit of the LB equation (1). Alternatively, the equilibrium was derived from the continuous Maxwell-Boltzmann distribution by expanding (in a Taylor series or Hermite basis) to the desired order [25,32]. The last and most recent approach for the derivation of the equilibrium is based on entropic construction, where one first discretizes the continuous entropy function $H = \int f \ln f dv$ and then computes the equilibrium as the point of minimum discrete entropy [12]. This contrasts with the second approach that first computes the equilibrium of the continuous H function (resulting in the Maxwell-Boltzmann distribution) and then discretizes it to attain the discrete equilibrium. This discretization obviously violates the entropy maximum condition that was valid for the Boltzmann equation [33]. Hence, the entropic approach is the only possibility of having a valid equilibrium that is defined as the point of maximum entropy, thus bringing thermodynamic consistency and stability to the LB scheme. It is worth noting that most expressions for equilibrium in the LB literature are polynomial in nature. Also, in the case of the entropic lattice Boltzmann method, the solution of the minimization of the discrete H function, although nonlinear, is written approximately as a polynomial in velocity (small perturbations around zero flow velocity). Polynomial equilibria suffer from two limitations, namely, limited positivity (the f_i^{eq} become negative at high Ma numbers) and inaccuracies at large values of flow velocities. Loss of positivity renders the physical nature of the populations void and is considered as one of the sources of numerical instabilities in the scheme [34]. Moreover, a polynomial that is obtained as an expanded solution to the entropic minimization problem cannot be used at large values of flow velocities, due to exponential divergence from the desired solution arising from the finite nature of the polynomials. Hence it is clear that any polynomial solution to the equilibrium cannot be used for high-Mach-number compressible flows. Thus, it is of quintessential importance that a method of evaluation of equilibrium is found for any possible extension of LB methods to high-velocity flows.

Here we proceed with the entropic definition of equilibrium that is derived by minimization of the discrete entropy function H [35],

$$H(f) = \sum_{i=1}^{n} f_i \ln\left(\frac{f_i}{W_i}\right), \tag{6}$$

where $W_i = W_i(T)$ are the temperature-dependent weights. In order to construct weights W_i, we start from the one-dimensional weights $w_{i\alpha}$, which are derived by matching the first $(n+1)/2$ nonvanishing Maxwell-Boltzmann moments at $u = 0$ and $\rho = 1$ [15,30]. In our specific case, for a D1Q7 lattice, the one-dimensional weights read

$$w_0 = \frac{36 - 49T + 42T^2 - 15T^3}{36}, \tag{7}$$

$$w_{\pm1} = \frac{T(12 - 13T + 5T^2)}{16}, \tag{8}$$

$$w_{\pm2} = \frac{T(-3 + 10T - 5T^2)}{40}, \tag{9}$$

$$w_{\pm3} = \frac{T(4 - 15T + 15T^2)}{720}, \tag{10}$$

where T is the flow temperature. The above relations imply a positivity window for T as $1 - \sqrt{2/5} < T < 1 + \sqrt{2/5}$ and a reference temperature of $T_0 = 0.697\,953$ [15,30]. The weight W_i of each discrete velocity $\boldsymbol{v}_i$ in the natural Cartesian reference frame $v_i = (v_{ix}, v_{iy}, v_{iz})$, $i\alpha \in 0,1,2,3$, is then the algebraic product of the corresponding one-dimensional weights

$$W_i = w_{ix} w_{iy} w_{iz}. \tag{11}$$

Minimization of H (6) is carried out under the constraints of local conservation of mass ρ, momentum $\rho\boldsymbol{u}$, and translational energy E_{tr} [Eq. (2)]. The minimization problem is solved with the method of the Lagrange multipliers (LMs), leading to

$$\delta H + \delta(\chi\rho + \boldsymbol{\zeta} \cdot (\rho\boldsymbol{u}) + \lambda\rho E_{\mathrm{tr}}) = 0, \tag{12}$$

where $\chi(\boldsymbol{u},T)$, $\boldsymbol{\zeta}(\boldsymbol{u},T)$, and $\lambda(\boldsymbol{u},T)$ are Lagrange multipliers corresponding to conservation of mass, momentum, and translational energy, respectively. The formal solution to the minimization problem reads

$$f_i^{\mathrm{eq}} = \rho W_i \exp\left(\chi + \boldsymbol{\zeta}\cdot\boldsymbol{v}_i + \lambda v_i^2\right). \tag{13}$$

The closed form of f_i^{eq} is computed by applying the conservation laws (2)–(13). This results in $D+2$ equations for $D+2$ unknown LMs, where D is the dimension of the problem. In the case of the standard lattice ($V_1 = \{0, \pm 1\}$) and isothermal flows, this leads to a quadratic system of equations, in terms of Lagrange multipliers, that was earlier solved analytically in [12]. However, for larger lattices, say, the D1Q5 and D1Q7 lattices (and the respective lattices in higher dimensions), and with energy conservation, this leads to a system of $D+2$ equations of the order $9D+3$, thus ruling out any possibility of computing them with an exact analytical solution. The main problem here reduces then in finding an appealing way of computing the exact entropic equilibrium for any given velocity and temperature for any lattice. The first application of entropy supporting higher-order lattices like in [17] for isothermal flows and in [18] for thermal flows employed an expanded version around zero velocity of the LM included in the equilibrium (13). This version of the entropic equilibrium, however, suffers the same problem of positivity as for the conventional polynomial when the velocity is increased.

We suggest here direct numerical evaluation of LMs using the rapidly converging Newton-Raphson method. Our simulations shows that such an approach converges to an accurate solution (with error of order 10^{-8}) with approximatively five iterations. The computational cost associated with such a numerical evaluation is not high when compared to the standard way of evaluating the equilibrium using polynomials. This is due to the fact that in spite of the usage of a large number of discrete velocities (7^2 in 2D and 7^3 in 3D) we have only four unknowns (LMs) in 2D and five unknowns in 3D, which then compares to the cost of computing 7^2 or 7^3 polynomials of the order $\boldsymbol{u}^4$. Furthermore, it must be remembered that a polynomial truncated to order $\boldsymbol{u}^4$ carries errors of order $\boldsymbol{u}^5$ and higher in the equilibrium moments, thus leading to large deviations from the desired moments values when velocity is increased. In our implementation, we have a comparable computational time between numerical and polynomial evaluation. It is worth noting that the positivity range for equilibrium now is greatly enhanced due to its exponential form of Eq. (13): The equilibrium is in fact always positive in the temperature range of positivity for the weights and until a speed at which the minimization problem admits real-valued solutions for the LM.

C. Compressible lattice Boltzmann equations

Armed with the above method of accurate evaluation of entropic equilibrium and a higher-order lattice that guarantees stability and an accurate evaluation of the Maxwell-Boltzmann moments until the fourth-order moment, the ELBM model for compressible flows is written in the standard propagation-relaxation form as

$$\begin{aligned} &f_i(\boldsymbol{x}+\boldsymbol{v}_i,t+1) - f_i(\boldsymbol{x},t) \\ &\quad = 2\beta_1\left(f_i^{\mathrm{eq}} - f_i\right) + 2(\beta_1-\beta_2)[f_i^* - f_i^{\mathrm{eq}}]. \end{aligned} \tag{14}$$

Note that (14) is a modification of Eq. (1) in order to control the Prandtl number as in [36], by modifying β_1 and β_2 independently, as shown below, and similarly to [37]. Here f_i^* is the quasiequilibrium population, which in the case of $\mathrm{Pr} < 1$ reads

$$f_i^* = f_i^{\mathrm{eq}} + W_i \overline{\boldsymbol{Q}} : [\boldsymbol{v}_i\otimes\boldsymbol{v}_i\otimes\boldsymbol{v}_i - 3T\boldsymbol{v}_i\boldsymbol{I}]/6T^3, \tag{15}$$

where

$$\overline{\boldsymbol{Q}} = \sum_{i=1}^{n} f_i(\boldsymbol{v}_i - \boldsymbol{u})\otimes(\boldsymbol{v}_i - \boldsymbol{u})\otimes(\boldsymbol{v}_i - \boldsymbol{u}) \tag{16}$$

is the centered heat flux tensor and $\boldsymbol{I}$ is the unit tensor. Note that with the quasiequilibrium (15), the present model differs from the well-known Shakov model where the once-contracted tensor $\overline{\boldsymbol{q}}$ is used instead of the tensor $\overline{\boldsymbol{Q}}$ [38]. Moreover, the model (14) is restricted to a fixed value of adiabatic exponent $\gamma_{\mathrm{tr}} = 5/3$ owing to the fact that f_i^{eq} was matched to the Maxwell-Boltzmann distribution for a monatomic gas. Previous approaches employed to make variable adiabatic exponent γ, such as in [39] or [40], are limited to models with a prescribed polynomial form of the equilibrium. Since our way of computing equilibrium is exact and needs numerical evaluation, we employ an alternative way by following the idea of [41,42] and introduce another set of populations g_i, which carry the energy related to the internal degrees of freedom (rotational and vibrational) and thus enabling a variable γ. The kinetic equation for g populations is written as

$$\begin{aligned} &g_i(\boldsymbol{x}+\boldsymbol{v}_i,t+1) - g_i(\boldsymbol{x},t) \\ &\quad = 2\beta_1\left(g_i^{\mathrm{eq}} - g_i\right) + 2(\beta_1-\beta_2)\left[g_i^* - g_i^{\mathrm{eq}}\right]. \end{aligned} \tag{17}$$

The equilibrium g_i^{eq} accounts for the conservation of the energy stored in the internal degrees of freedom

$$2\rho E_{\mathrm{int}} = \sum_{i=1}^{n} g_i^{\mathrm{eq}} = (2C_v - D)\rho T, \tag{18}$$

where C_v is the specific heat at constant volume. The conservation law for the total energy becomes

$$2\rho E_{\mathrm{tot}} = 2C_v\rho T + \rho u^2 = \sum_{i=1}^{n} v_i^2 f_i^{\mathrm{eq}} + \sum_{i=1}^{n} g_i^{\mathrm{eq}} \tag{19}$$

and the adiabatic exponent is related to a variable specific heat at constant volume C_v by $\gamma = (C_v+1)/C_v$. Note that the equilibrium g_i^{eq} need not be computed by another Newton-Raphson iterative operation; once f_i^{eq} is evaluated, we set

$$g_i^{\mathrm{eq}} = (2C_v - D)T f_i^{\mathrm{eq}}. \tag{20}$$

The quasiequilibrium g_i^* is defined consistently with f_i^* as

$$g_i^* = g_i^{\mathrm{eq}} + W_i \overline{\boldsymbol{q}}\cdot\boldsymbol{v}_i/T, \tag{21}$$

where

$$\overline{\boldsymbol{q}} = \sum_{i=1}^{n} g_i(\boldsymbol{v}_i - \boldsymbol{u}) \tag{22}$$

is the contracted and centered heat flux tensor associated with the internal degrees of freedom.

D. Thermohydrodynamic limit of the compressible ELBM

We proceed here by deriving the thermohydrodynamic limit of Eqs. (14) and (17) for the case of a D-dimensional gas characterized by a Prandtl number $\mathrm{Pr} \leqslant 1$; for Prandtl $\mathrm{Pr} > 1$ the procedure is similar and can be found in [18]. The thermohydrodynamic limit is derived using the Chapman-Enskog method, under the assumption that the second-, third-, and fourth-order Maxwell-Boltzmann moments are recovered by the equilibrium populations, as shown in Sec. II A. We start by expanding the shift operator of Eqs. (14) and (17) in a Taylor series up to second order,

$$\left[\delta t(\partial_t + \partial_\mu c_{i\mu}) + \frac{\delta t^2}{2}(\partial_t + \partial_\mu c_{i\mu})(\partial_t + \partial_\nu c_{i\nu})\right] f_i = 2\beta_1\left(f_i^{\mathrm{eq}} - f_i\right) + 2(\beta_1 - \beta_2)\left[f_i^* - f_i^{\mathrm{eq}}\right], \tag{23}$$

$$\left[\delta t(\partial_t + \partial_\mu c_{i\mu}) + \frac{\delta t^2}{2}(\partial_t + \partial_\mu c_{i\mu})(\partial_t + \partial_\nu c_{i\nu})\right] g_i = 2\beta_1\left(g_i^{\mathrm{eq}} - g_i\right) + 2(\beta_1 - \beta_2)\left[g_i^* - g_i^{\mathrm{eq}}\right], \tag{24}$$

and by introducing a characteristic time scale of the flows Θ and a reduced time $t' = t/\Theta$. Similarly, we introduce reduced velocities and reduced coordinate $v_i' = v_i/c$ and $x' = x/c\Theta$, respectively, where $c = 1$, and we rewrite Eqs. (23) and (24) in terms of the reduced variables t' and x' and drop primes to simplify notation. After introduction of the smallness parameter $\epsilon = \delta t/\Theta$, Eqs. (23) and (24) can be written as

$$\left[\epsilon(\partial_t + \partial_\mu c_{i\mu}) + \frac{\epsilon^2}{2}(\partial_t + \partial_\mu c_{i\mu})(\partial_t + \partial_\nu c_{i\nu})\right] f_i = 2\beta_1\left(f_i^{\mathrm{eq}} - f_i\right) + 2(\beta_1 - \beta_2)\left[f_i^* - f_i^{\mathrm{eq}}\right], \tag{25}$$

$$\left[\epsilon(\partial_t + \partial_\mu c_{i\mu}) + \frac{\epsilon^2}{2}(\partial_t + \partial_\mu c_{i\mu})(\partial_t + \partial_\nu c_{i\nu})\right] g_i = 2\beta_1\left(g_i^{\mathrm{eq}} - g_i\right) + 2(\beta_1 - \beta_2)\left[g_i^* - g_i^{\mathrm{eq}}\right]. \tag{26}$$

We can now perform a multiscale expansion of the time derivative operator, of the populations, and of the quasiequilibrium f and g populations, to second order as

$$\epsilon\partial_t = \epsilon\partial_t^{(1)} + \epsilon^2\partial_t^{(2)} + \cdots, \tag{27}$$

$$f_i = f_i^{(0)} + \epsilon f_i^{(1)} + \epsilon^2 f_i^{(2)} + \cdots, \tag{28}$$

$$g_i = g_i^{(0)} + \epsilon g_i^{(1)} + \epsilon^2 g_i^{(2)} + \cdots, \tag{29}$$

$$f_i^* = f_i^{*(0)} + \epsilon f_i^{*(1)} + \epsilon^2 f_i^{*(2)} + \cdots, \tag{30}$$

$$g_i^* = g_i^{*(0)} + \epsilon g_i^{*(1)} + \epsilon^2 g_i^{*(2)} + \cdots. \tag{31}$$

Inserting Eqs. (27), (28), and (30) into Eq. (25), and Eqs. (27), (29), and (31) into Eq. (26), an analysis to orders $\epsilon^{(0)}$, $\epsilon^{(1)}$, and $\epsilon^{(2)}$ is performed.

1. Zeroth-order terms

Terms to the order $\epsilon^{(0)}$ lead to

$$f_i^{(0)} = f_i^{*(0)} + \frac{\beta_2}{\beta_1}\left(f_i^{\mathrm{eq}} - f_i^{*(0)}\right) \tag{32}$$

and

$$g_i^{(0)} = g_i^{*(0)} + \frac{\beta_2}{\beta_1}\left(g_i^{\mathrm{eq}} - g_i^{*(0)}\right). \tag{33}$$

Since $f_i^{*(0)}$ and $g_i^{*(0)}$ are chosen to satisfy

$$\sum_{i=1}^{n}\left\{1, \boldsymbol{v}_i, v_i^2/2\right\} f_i^{*(0)} = \sum_{i=1}^{n}\left\{1, \boldsymbol{v}_i, v_i^2/2\right\} f_i^{\mathrm{eq}} \tag{34}$$

and

$$\sum_{i=1}^{n} g_i^{*(0)} = \sum_{i=1}^{n} g_i^{\mathrm{eq}}, \tag{35}$$

we find that the leading term in the expansions (28) and (29) is the local equilibrium

$$f_i^{(0)} = f_i^{\mathrm{eq}}, \quad g_i^{(0)} = g_i^{\mathrm{eq}}. \tag{36}$$

Local conservation laws imply

$$\sum_{i=0}^{n}\{1, v_{i\alpha}\} f_i = \sum_{i=0}^{n}\{1, v_{i\alpha}\} f_i^{\mathrm{eq}} \tag{37}$$

for mass and momentum conservation and

$$\sum_{i=0}^{n}\left(v_i^2 f_i + g_i\right) = \sum_{i=0}^{n}\left(v_i^2 f_i^{\mathrm{eq}} + g_i^{\mathrm{eq}}\right) \tag{38}$$

for the total energy conservation, which, combined with Eqs. (28), (29), and (36) lead to the solvability conditions

$$\sum_{i=0}^{n}\{1, v_{i\alpha}\} f_i^{(1)} = \sum_{i=0}^{n}\{1, v_{i\alpha}\} f_i^{(2)} = \cdots = 0 \tag{39}$$

and

$$\sum_{i=0}^{n}\left(v_i^2 f_i^{(1)} + g_i^{(1)}\right) = \sum_{i=0}^{n}\left(v_i^2 f_i^{(2)} + g_i^{(2)}\right) = \cdots = 0. \tag{40}$$

2. First-order terms

Collecting terms to the order $\epsilon^{(1)}$, we obtain an expression for the first-order f and g populations

$$f_i^{(1)} = f_i^{*(1)}\left(1 - \frac{\beta_2}{\beta_1}\right) - \frac{1}{2\beta_1}\left(\partial_t^{(1)} + \partial_\mu v_{i\mu}\right) f_i^{(0)}, \tag{41}$$

$$g_i^{(1)} = g_i^{*(1)}\left(1 - \frac{\beta_2}{\beta_1}\right) - \frac{1}{2\beta_1}\left(\partial_t^{(1)} + \partial_\mu v_{i\mu}\right) g_i^{(0)}. \tag{42}$$

Applying solvability conditions (39) to Eq. (41) and using the conditions

$$\sum_{i=0}^{n}\{1, v_{i\alpha}\} f_i^{*(1)} = 0 \tag{43}$$

obtained from (34) for the quasiequilibrium populations, the thermohydrodynamic equations of mass and momentum are recovered to first order:

$$\partial_t^{(1)}\rho = -\partial_\alpha(\rho u_\alpha), \tag{44}$$

$$\partial_t^{(1)} u_\alpha = -u_\beta\partial_\beta u_\alpha - \frac{1}{\rho}\partial_\alpha(\rho T). \tag{45}$$

The term ρT can be identified as $p = \rho T$, which is the equation of state for ideal gases, with p being the pressure. In order to obtain first-order equations for the total energy, we need to apply the solvability condition (40) to the sum of Eqs. (41) and (42) and use the condition [from (34)]

$$\sum_{i=0}^{n}\left(v_i^2 f_i^{*(1)} + g_i^{*(1)}\right) = 0, \tag{46}$$

so that

$$\partial_t^{(1)} T = -u_\alpha \partial_\alpha T - \frac{1}{\rho C_v}\rho T(\partial_\alpha u_\alpha). \tag{47}$$

3. *Second-order terms*

We proceed now by collecting terms of order $\epsilon^{(2)}$ in Eqs. (25) and (26):

$$\begin{aligned}&\left[\partial_t^{(2)} + \tfrac{1}{2}\left(\partial_t^{(1)}\partial_t^{(1)} + \partial_\mu\partial_\nu v_{i\mu}v_{i\nu} + 2\partial_t^{(1)}\partial_\mu v_{i\mu}\right)\right] f_i^{(0)}\\ &\quad = -2\beta_1 f_i^{(2)} - 2(\beta_2 - \beta_1) f_i^{*(2)} - \left(\partial_t^{(1)} + \partial_\mu v_{i\mu}\right) f_i^{(1)},\end{aligned} \tag{48}$$

$$\begin{aligned}&\left[\partial_t^{(2)} + \tfrac{1}{2}\left(\partial_t^{(1)}\partial_t^{(1)} + \partial_\mu\partial_\nu v_{i\mu}v_{i\nu} + 2\partial_t^{(1)}\partial_\mu v_{i\mu}\right)\right] g_i^{(0)}\\ &\quad = -2\beta_1 g_i^{(2)} - 2(\beta_2 - \beta_1) g_i^{*(2)} - \left(\partial_t^{(1)} + \partial_\mu v_{i\mu}\right) g_i^{(1)}.\end{aligned} \tag{49}$$

Applying Eq. (41) in (48) and Eq. (42) in (49) and considering that $f_i^{*,(2)} = g_i^{*,(2)} = 0$ by construction of the quasiequilibrium, Eqs. (48) and (49) become

$$\begin{aligned}&\left[\partial_t^{(2)} - \left(\frac{1}{2\beta_1} - \frac{1}{2}\right)\left(\partial_t^{(1)}\partial_t^{(1)} + \partial_\mu\partial_\nu v_{i\mu}v_{i\nu} + 2\partial_t^{(1)}\partial_\mu v_{i\mu}\right)\right] f_i^{(0)}\\ &= -2\beta_1 f_i^{(2)} - \left(\partial_t^{(1)} + \partial_\mu v_{i\mu}\right) f_i^{*(1)}\left(1 - \frac{\beta_2}{\beta_1}\right),\end{aligned} \tag{50}$$

$$\begin{aligned}&\left[\partial_t^{(2)} - \left(\frac{1}{2\beta_1} - \frac{1}{2}\right)\left(\partial_t^{(1)}\partial_t^{(1)} + \partial_\mu\partial_\nu v_{i\mu}v_{i\nu} + 2\partial_t^{(1)}\partial_\mu v_{i\mu}\right)\right] g_i^{(0)}\\ &= -2\beta_1 g_i^{(2)} - \left(\partial_t^{(1)} + \partial_\mu v_{i\mu}\right) g_i^{*(1)}\left(1 - \frac{\beta_2}{\beta_1}\right).\end{aligned} \tag{51}$$

Applying the solvability condition for the mass, we obtain a vanishing second-order contribution to the continuity equation

$$\partial_t^{(2)}\rho = 0. \tag{52}$$

Applying the solvability condition for the momentum to (50) and the solvability condition for the total energy to (50) and (51), we find

$$\begin{aligned}\partial_t^{(2)}(\rho u_\alpha) &= \left(\frac{1}{2\beta_1} - \frac{1}{2}\right)\partial_\beta\left(\partial_t^{(1)} P_{\alpha\beta}^{\text{eq}} + \partial_\gamma Q_{\alpha\beta\gamma}^{\text{eq}}\right)\\ &\quad - \left(1 - \frac{\beta_2}{\beta_1}\right)\partial_\beta P_{\alpha\beta}^{*(1)},\end{aligned} \tag{53}$$

$$\begin{aligned}\partial_t^{(2)}(2\rho E) &= \left(\frac{1}{2\beta_1} - \frac{1}{2}\right)\partial_\alpha\left(\partial_t^{(1)} q_\alpha^{\text{eq}} + \partial_\beta R_{\alpha\beta}^{\text{eq}}\right)\\ &\quad - \left(1 - \frac{\beta_2}{\beta_1}\right)\partial_\alpha q_\alpha^{*(1)}.\end{aligned} \tag{54}$$

As anticipated, in the case where $\text{Pr} < \text{Pr}_{\text{BGK}}$, the additional quasiconserved quantity for the quasiequilibrium population is the centered heat transfer tensor $\overline{Q}_{\alpha\beta\gamma}$, i.e.,

$$f^* = f^*(\rho, u_\alpha, \rho E_{\text{tr}}, \overline{Q}_{\alpha\beta\gamma}). \tag{55}$$

This additional conservation guarantees the following form for the first-order heat flux and the first-order pressure tensor:

$$q_\alpha^{*(1)} = q_\alpha^{(1)} - 2u_\gamma P_{\alpha\gamma}^{(1)}, \tag{56}$$

$$P_{\alpha\beta}^{*(1)} = 0. \tag{57}$$

By projecting Eqs. (41) and (42) on the desired moment space, it is possible to obtain $q_\alpha^{(1)}$ as

$$q_\alpha^{(1)} = q_\alpha^{*(1)}\left(1 - \frac{\beta_2}{\beta_1}\right) - \frac{1}{2\beta_1}\left(\partial_t^{(1)} q_\alpha^{\text{eq}} + \partial_\beta R_{\alpha\beta}^{\text{eq}}\right) \tag{58}$$

and, by using (57), the first-order pressure tensor $P_{\alpha\beta}^{(1)}$,

$$P_{\alpha\beta}^{(1)} = -\frac{1}{2\beta_1}\left(\partial_t^{(1)} P_{\alpha\beta}^{\text{eq}} + \partial_\gamma Q_{\alpha\beta\gamma}^{\text{eq}}\right). \tag{59}$$

By inserting (59) in (56) and (56) in (58), we obtain an expression for $q_\alpha^{*(1)}$:

$$q_\alpha^{*(1)} = -\frac{1}{2\beta_2}\left(\partial_t^{(1)} q_\alpha^{\text{eq}} + \partial_\beta R_{\alpha\beta}^{\text{eq}}\right) - \frac{2u_\beta}{2\beta_2}\left(\partial_t^{(1)} P_{\alpha\beta}^{\text{eq}} + \partial_\gamma Q_{\alpha\beta\gamma}^{\text{eq}}\right). \tag{60}$$

Computing explicitly the right-hand side of Eq. (60) we obtain

$$q_\alpha^{*(1)} = -\frac{1}{2\beta_2}(C_v + 1)\rho T\partial_\alpha T, \tag{61}$$

where $C_p = C_v + 1$ is the heat capacity at constant pressure. At this point, the computation of the second-order time derivative of momentum and energy is straightforward: Using (57) we obtain the second-order momentum equation

$$\partial_t^{(2)} u_\alpha = -\frac{1}{\rho}\partial_\beta \Pi_{\alpha\beta}, \tag{62}$$

where $\Pi_{\alpha\beta}$ is the stress tensor

$$\Pi_{\alpha\beta} = -\mu\left(S_{\alpha\beta} - \frac{2}{D}\partial_\gamma u_\gamma \delta_{\alpha\beta}\right) + \xi\partial_\gamma u_\gamma \delta_{\alpha\beta}, \tag{63}$$

with

$$S_{\alpha\beta} = \partial_\alpha u_\beta + \partial_\beta u_\alpha \tag{64}$$

the strain rate tensor,

$$\mu = \left(\frac{1}{2\beta_1} - \frac{1}{2}\right)\rho T \tag{65}$$

the dynamic viscosity, and

$$\xi = \left(\frac{1}{C_v} - \frac{2}{D}\right)\mu \tag{66}$$

the bulk viscosity, characteristic of any kinetic scheme with an internal degrees of freedom $C_v \neq D/2$. The left-hand side of Eq. (54) is transformed using second-order time derivatives of mass and momentum [Eqs. (52) and (62)]

$$\partial_t^{(2)}(\rho E) = \rho C_v \partial_t^{(2)} T - u_\alpha \partial_\beta \Pi_{\alpha\beta}. \tag{67}$$

The right-hand side of Eq. (54) is transformed by computing explicitly the first-order time derivative of q_α^{eq} and the spatial derivative of $R_{\alpha\beta}^{\mathrm{eq}}$; by making use of Eqs. (44), (45), (47), and (61) we obtain

$$\partial_t^{(1)} q_\alpha^{\mathrm{eq}} + \partial_\beta R_{\alpha\beta}^{\mathrm{eq}} = (C_v + 1)\rho T \partial_\alpha T + \rho T u_\beta \left(S_{\alpha\beta} - \frac{1}{C_v}(\partial_\gamma u_\gamma)\delta_{\alpha\beta} \right). \tag{68}$$

By substitution of (68) and (67) in (54) we obtain the second-order derivative of the temperature

$$\partial_t^{(2)} T = \frac{1}{\rho C_v}\partial_\alpha(\kappa \partial_\alpha T) - \frac{1}{\rho C_v}(\partial_\alpha u_\beta)\Pi_{\alpha\beta}, \tag{69}$$

where κ is the thermal conductivity given by

$$\kappa = C_p\left(\frac{1}{2\beta_2} - \frac{1}{2}\right)\rho T. \tag{70}$$

4. Thermohydrodynamic equations

Summing up contributions of first and second order, the Fourier-Navier-Stokes equations for compressible flows are recovered as follows:

$$\partial_t \rho + \partial_\alpha(\rho u_\alpha) = 0, \tag{71}$$

$$\partial_t u_\alpha + u_\beta \partial_\beta u_\alpha = -\frac{1}{\rho}\partial_\alpha(\rho T) - \frac{1}{\rho}\partial_\beta \Pi_{\alpha\beta}, \tag{72}$$

$$\partial_t T = -u_\alpha \partial_\alpha T - \frac{1}{\rho C_v}\rho T(\partial_\alpha u_\alpha) - \frac{1}{\rho C_v}(\partial_\alpha u_\beta)\Pi_{\alpha\beta} + \frac{1}{\rho C_v}\partial_\alpha(\kappa \partial_\alpha T), \tag{73}$$

where, as before, the stress tensor is defined as

$$\Pi_{\alpha\beta} = -\mu\left(S_{\alpha\beta} - \frac{2}{D}\partial_\gamma u_\gamma \delta_{\alpha\beta}\right) + \xi \partial_\gamma u_\gamma \delta_{\alpha\beta},$$

with the strain rate tensor

$$S_{\alpha\beta} = \partial_\alpha u_\beta + \partial_\beta u_\alpha.$$

Expressions for dynamic viscosity, bulk viscosity, thermal conductivity, and adiabatic exponent are given by, respectively,

$$\mu = \left(\frac{1}{2\beta_1} - \frac{1}{2}\right)\rho T, \quad \xi = \left(\frac{1}{C_v} - \frac{2}{D}\right)\mu,$$

$$\kappa = C_p\left(\frac{1}{2\beta_2} - \frac{1}{2}\right)\rho T, \quad \gamma = \frac{C_p}{C_v}$$

and the expression for the Prandtl number becomes

$$\mathrm{Pr} = \frac{(1-\beta_1)\beta_2}{(1-\beta_2)\beta_1}. \tag{74}$$

E. Entropic estimate for improved numerical stability

Since the LBGK models allow limited stability for high-Reynolds-number flows, we extend here the kinetic equations (14) and (17) to their entropic variant based on [35]:

$$f_i(\boldsymbol{x} + \boldsymbol{v}_i, t+1) - f_i(\boldsymbol{x}, t) = \alpha\beta_1\left(f_i^{\mathrm{eq}} - f_i\right) + 2(\beta_1 - \beta_2)\left[f_i^* - f_i^{\mathrm{eq}}\right], \tag{75}$$

$$g_i(\boldsymbol{x} + \boldsymbol{v}_i, t+1) - g_i(\boldsymbol{x}, t) = \alpha\beta_1\left(g_i^{\mathrm{eq}} - g_i\right) + 2(\beta_1 - \beta_2)\left[g_i^* - g_i^{\mathrm{eq}}\right]. \tag{76}$$

In the above equations, equilibrium populations f_i^{eq} and g_i^{eq} are the same as in Secs. II B and II C, while the relaxation parameter related to the viscosity is replaced by $\alpha\beta_1$, where α is the maximal overrelaxation parameter, which is the positive root of the entropy condition

$$H(f + \alpha(f^{\mathrm{eq}} - f)) = H(f), \tag{77}$$

where H is the entropy function (6). This formulation is based on the assumption that the entropic estimate (77) serves to stabilize the flow only through viscosity, without affecting the thermal conductivity.

The entropic relaxation parameter α was originally conceived for stabilization of high-Reynolds-number flow simulations to handle large velocity gradients [33]. In that case, fluctuations of α around $\alpha = 2$ due to the entropic estimate acts as a built-in subgrid model. The entropic relaxation parameter α then played a crucial role in stabilizing multiphase flow simulations with large density gradients [43]. It will be shown below that the entropic estimate helps to stabilize the compressible flow simulations where large gradients of velocity, density, and temperature are present. The stabilizing effect of the entropic estimate is triggered automatically and is of importance for two reasons: In the turbulent regions the entropic estimate acts as a built-in subgrid model as it would be for incompressible flows, and in the presence of shocks, it naturally helps avoiding the Gibbs oscillations that would otherwise corrupt the flow field. It is remarkable that the entire scheme described thus far is free of any tuning parameter and the required stabilization of the flows occurs automatically by simply respecting the second law of thermodynamic, without the need to identify the regions that would destabilize the simulations.

1. Implementation details

In order to solve Eq. (77), the first step of the implementation consists in checking the allowable values for α guaranteeing that the discrete H function (6) can be evaluated, i.e.,

$$f_i + \alpha\left(f_i^{\mathrm{eq}} - f_i\right) > 0. \tag{78}$$

Assuming that populations f_i are always positive, the positivity condition (78) translates to the values for minimum and maximum entropic estimates as

$$\begin{aligned} \alpha_{\min} &= \max\{\delta_i, i \in 1,2,\ldots,Q \quad \text{if } \delta_i < 0\}, \\ \alpha_{\max} &= \min\{\delta_i, i \in 1,2,\ldots,Q \quad \text{if } \delta_i > 0\}, \end{aligned} \tag{79}$$

where $\delta_i = \frac{f_i}{f_i - f_i^{\mathrm{eq}}}$. In the case $\alpha_{\max} < \alpha_{\mathrm{LBGK}}\ (= 2)$ we directly set $\alpha = \alpha_{\max}$; otherwise, Eq. (77) is solved with the Newton-Raphson method for α.

F. Realization of the compressible ELBM

We now summarize the equations and expressions needed for the implementation of the compressible entropic LB model. The two kinetic lattice Boltzmann equations including quasiequilibrium model read

$$\begin{aligned} f_i(\boldsymbol{x}+\boldsymbol{c}_i\delta t,t+\delta t)-f_i(\boldsymbol{x},t) \\ =\alpha\beta_1(f_i^*-f_i)+2\beta_2\big(f_i^{\text{eq}}-f_i^*\big), \end{aligned} \tag{80}$$

$$\begin{aligned} g_i(\boldsymbol{x}+\boldsymbol{c}_i\delta t,t+\delta t)-g_i(\boldsymbol{x},t) \\ =\alpha\beta_1(g_i^*-g_i)+2\beta_2\big(g_i^{\text{eq}}-g_i^*\big), \end{aligned} \tag{81}$$

where the equilibrium f_i^{eq} is computed by solving numerically the equations

$$\left\{\rho,\rho\boldsymbol{u},\frac{3}{2}\rho T+\rho\boldsymbol{u}^2\right\}=\sum_{i=1}^{n}\left\{1,\boldsymbol{v}_i,v_i^2/2\right\}f_i^{\text{eq}}(\rho,\boldsymbol{u},T) \tag{82}$$

for χ, ζ_α, and λ in

$$f_i^{\text{eq}}=\rho W_i\exp\left(\chi+\zeta_\alpha v_{i\alpha}+\lambda v_i^2\right), \tag{83}$$

while the equilibrium g_i^{eq} is consequently given by

$$g_i^{\text{eq}}=(2C_v-D)Tf_i^{\text{eq}}. \tag{84}$$

It must be noted that Eq. (1) together with f_i^{eq} defined as Eqs. (82) and (83) can also be used for simulation of compressible flows at $\text{Pr}=1$, $\gamma=(D+2)/D$, and low-Reynolds-number flows. Moreover, for thermal low-Mach-number problems, the current approach can be used to recover the results of [18] with the V_5 and V_7 lattices. We do not present here low-Mach-number simulations. Instead, only flows with significant compressibility effects are presented.

Quasiequilibrium f populations can be written in the compact form as

$$f_i^*=f_i^{\text{eq}}+\frac{W_i\overline{\boldsymbol{Q}}:[\boldsymbol{v}_i\otimes\boldsymbol{v}_i\otimes\boldsymbol{v}_i-3T\boldsymbol{v}_i\boldsymbol{I}]}{6T^3}, \tag{85}$$

where

$$\overline{\boldsymbol{Q}}=\sum_{i=1}^{n}f_i(\boldsymbol{v}_i-\boldsymbol{u})\otimes(\boldsymbol{v}_i-\boldsymbol{u})\otimes(\boldsymbol{v}_i-\boldsymbol{u}). \tag{86}$$

The quasiequilibrium g population reads

$$g_i^*=g_i^{\text{eq}}+\frac{W_i\overline{\boldsymbol{q}}\cdot\boldsymbol{v}_i}{T}, \tag{87}$$

where the contracted centered third-order moment is

$$\overline{\boldsymbol{q}}=\sum_{i=1}^{n}g_i(\boldsymbol{v}_i-\boldsymbol{u}) \tag{88}$$

and $W_i(T)$ is the weight computed according to (11). The velocity set is composed of 20 energy shells (in 3D) that are constructed as the tensor products of D copies of one-dimensional velocity sets V_7, where

$$V_7=\{0,\pm1,\pm2,\pm3\}, \tag{89}$$

which leads to 343 velocities in three dimensions $D=3$.

The relaxation parameters β_1 and β_2 are computed by the corresponding dynamic viscosity and thermal conductivity

$$\beta_1=\frac{1}{\frac{2\mu}{\rho T}+1}, \tag{90}$$

$$\beta_2=\frac{1}{\frac{2\kappa}{\rho(C_v+1)T}+1} \tag{91}$$

and the heat capacity C_v is derived from the desired adiabatic exponent γ from

$$C_v=\frac{1}{\gamma-1}. \tag{92}$$

Finally, the compressible ELBM algorithm is summarized in three main steps.

(i) Propagation. Populations associated with discrete velocities $\boldsymbol{v}_i$ are moved to the corresponding adjacent links

$$f_i(\boldsymbol{x},t)\rightarrow f_i(\boldsymbol{x}+\boldsymbol{v}_i,t+1), \tag{93}$$

$$g_i(\boldsymbol{x},t)\rightarrow g_i(\boldsymbol{x}+\boldsymbol{v}_i,t+1), \tag{94}$$

which results in a new set of populations $f_i'(\boldsymbol{x},t)$ and $g_i'(\boldsymbol{x},t)$.

(ii) Wall boundary conditions. In the presence of walls, the missing populations at the wall are replaced according to the description given below in Sec. II G.

(iii) Collision step. In this last step, populations $f_i'(\boldsymbol{x},t)$ and $g_i'(\boldsymbol{x},t)$ are updated by the rule

$$\begin{aligned} f_i'(\boldsymbol{x},t)\leftarrow f_i'(\boldsymbol{x},t)+\alpha\beta_1\big(f_i^{\text{eq}}-f_i'\big) \\ +2(\beta_1-\beta_2)\big(f_i^*-f_i^{\text{eq}}\big), \end{aligned} \tag{95}$$

$$\begin{aligned} g_i'(\boldsymbol{x},t)\leftarrow g_i'(\boldsymbol{x},t)+\alpha\beta_1\big(g_i^{\text{eq}}-g_i'\big) \\ +2(\beta_1-\beta_2)\big(g_i^*-g_i^{\text{eq}}\big), \end{aligned} \tag{96}$$

where the two relaxation parameters, equilibrium populations and quasiequilibrium populations, have been previously described.

G. Boundary conditions for the compressible ELBM

The boundary conditions employed in the present compressible ELBM model are an extension to those presented in [18,44]. In general, the population $f_i(\boldsymbol{x}_b,t)$ [and $g_i(\boldsymbol{x}_b,t)$] associated with a boundary node residing in the fluid domain $\boldsymbol{x}_b$ (black and gray in Fig. 2) may belong to two different subsets, namely, the subset $\overline{D}$ denoting velocities pointing

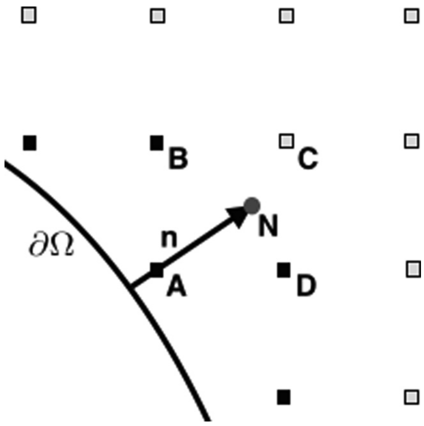

FIG. 2. Scheme representing boundary nodes (black $\boldsymbol{x}_{b,n}$ and gray $\boldsymbol{x}_{b,f}$) and normal $\boldsymbol{n}$ of the wall. Point N is employed to extrapolate flow-field values in the direction normal to the wall. A, B, C, and D are the points employed in the bilinear interpolation to compute N.

from the solid into the fluid domain and the subset of velocities pointing from the fluid into the solid or fluid domain.

Populations belonging to $\overline{D}$, $f_i(\boldsymbol{x}_b,t) \in \overline{D}$, are missing and need to be approximated in order to complete the advection step. Due to the employment of a multispeed lattice, we distinguish here between those nodes belonging to the boundary that are the nearest to the wall $\boldsymbol{x}_{b,n}$ (black in Fig. 2) and the nodes belonging to the boundary set that are only next to nearest $\boldsymbol{x}_{b,f}$ (gray in Fig. 2). Formally, they are distinguished by the following criterion: If

$$\max(\|\boldsymbol{r}\|_i, i \notin \overline{D}) \leqslant 1 \rightarrow \boldsymbol{x}_{b,n}; \tag{97}$$

otherwise

$$\max(\|\boldsymbol{r}\|_i, i \notin \overline{D}) > 1 \rightarrow \boldsymbol{x}_{b,f}, \tag{98}$$

where $\boldsymbol{r}_i = \boldsymbol{x}_b - \boldsymbol{x}_{w,i}$ and $\boldsymbol{x}_{w,i}$ is the intersection point of lattice link $\boldsymbol{v}_i$ with the wall.

We first proceed by specifying that only missing populations are replaced, for both $\boldsymbol{x}_{b,n}$ and $\boldsymbol{x}_{b,f}$ nodes. At this point, we need to formulate an approximation for the missing populations $f_i(\boldsymbol{x}_b,t)$ and $g_i(\boldsymbol{x}_b,t)$ at boundary node $\boldsymbol{x}_b$; we propose to approximate them by a chosen equilibrium part and a nonequilibrium part, approximated by the first-order Chapman-Enskog solution in the populations, leading to

$$f_i = f_i^{\mathrm{eq}}(\rho_{\mathrm{tgt}},\boldsymbol{u}_{\mathrm{tgt}},T_{\mathrm{tgt}}) + f_i^{(1)}(\rho_{\mathrm{tgt}},\boldsymbol{u}_{\mathrm{tgt}},T_{\mathrm{tgt}},\nabla\boldsymbol{u}_{\mathrm{tgt}},\nabla T_{\mathrm{tgt}}), \tag{99}$$

$$g_i = g_i^{\mathrm{eq}}(\rho_{\mathrm{tgt}},\boldsymbol{u}_{\mathrm{tgt}},T_{\mathrm{tgt}}) + g_i^{(1)}(\rho_{\mathrm{tgt}},\boldsymbol{u}_{\mathrm{tgt}},T_{\mathrm{tgt}},\nabla\boldsymbol{u}_{\mathrm{tgt}},\nabla T_{\mathrm{tgt}}), \tag{100}$$

where ρ_{tgt}, $\boldsymbol{u}_{\mathrm{tgt}}$, T_{tgt}, $\nabla\boldsymbol{u}_{\mathrm{tgt}}$, and ∇T_{tgt} are the target density, velocity, temperature, velocity Jacobian, and temperature gradient, respectively, that need to be specified. Before we proceed with specifying target values, the approximation for the first-order part of both f and g populations needs to be provided. For f populations, we use Grad's approximation of the form

$$f_i^{(1)} = W_i\left\{P_{\alpha\beta}^{(1)}\frac{v_{i,\alpha}v_{i,\beta} - T\delta_{\alpha\beta}}{2T^2} + Q_{\alpha\beta\gamma}^{(1)}\frac{v_{i,\alpha}v_{i,\beta}v_{i,\gamma} - 3v_{i,\gamma}T\delta_{\alpha\beta}}{6T^3}\right\}, \tag{101}$$

where $P_{\alpha\beta}^{(1)}$ and $Q_{\alpha\beta\gamma}^{(1)}$ are the first-order pressure tensor and heat flux tensor. First-order pressure and heat flux tensors are derived from Chapman-Enskog analysis, thus by projecting Eq. (41) to the second- and third-order moment space

$$P_{\alpha\beta}^{(1)} = -\frac{1}{2\beta_1}\rho T\left(S_{\alpha\beta} - \frac{1}{C_v}\partial_\gamma u_\gamma\delta_{\alpha\beta}\right), \tag{102}$$

where $S_{\alpha\beta}$ is given by Eq. (64) and

$$Q_{\alpha\beta\gamma}^{(1)} = -\frac{1}{2\beta_2}\rho T[\partial_\alpha T\delta_{\beta\gamma} + \partial_\beta T\delta_{\alpha\gamma} + \partial_\gamma T\delta_{\alpha\beta}] + u_\alpha P_{\beta\gamma}^{(1)} + u_\beta P_{\alpha\gamma}^{(1)} + u_\gamma P_{\alpha\beta}^{(1)}. \tag{103}$$

For g populations, we use Grad's approximation of the form

$$g_i^{(1)} = W_i\left\{\mathrm{Tr}^{(1),g} + \frac{v_{i,\alpha}}{T}q_\alpha^{(1),g} + \frac{X_{i,\alpha\beta}}{2T^2}R_{\alpha\beta}^{(1),g}\right\}, \tag{104}$$

where

$$\mathrm{Tr}^{(1),g} = \sum_{i=1}^{n} g_i^{(1)} \tag{105}$$

is the first-order contribution of the zeroth-order moment of the g populations, $q_\alpha^{(1),g}$ is the first-order contribution to the contracted heat flux associated with g populations, and $R_{\alpha\beta}^{(1),g}$ is the first-order contribution to the contracted fourth-order moment of g populations. All these moments can be derived analytically by the Chapman-Enskog method, thus by projecting Eq. (42) to desired order moment

$$\mathrm{Tr}^{(1)} = -\frac{1}{2\beta_1}\rho T(2C_v - D)\left(\frac{1}{C_v}\partial_\gamma u_\gamma\right), \tag{106}$$

$$q_\alpha^{(1),g} = -\frac{1}{2\beta_2}\rho T(2C_v - D)\partial_\alpha T + Tr^{(1)}u_\alpha, \tag{107}$$

$$R_{\alpha\beta}^{(1),g} = -\frac{1}{2\beta_1}\rho T(2C_v - D)(TS_{\alpha\beta} + u_\alpha\partial_\beta T + u_\beta\partial_\alpha T). \tag{108}$$

At this point, we need to specify target values. The target values need to be chosen based on which type of boundary conditions one wants to simulate: inlet, no-slip, or free-slip (which includes adiabatic wall treatment for the temperature) boundary condition. For the case of the outlet boundary condition we proceed alternatively by replacing all populations belonging to the outlet by previous time-step populations. Before proceeding with the description of target quantities, we want to stress that only target quantities belonging to $\boldsymbol{x}_{b,n}$ boundary nodes need to be specified, while for the boundary nodes $\boldsymbol{x}_{b,f}$ we employ previous time step local quantities. Temperature gradients and velocity Jacobian are instead evaluated by a second-order centered scheme, based on previous time step quantities. For the case of the inlet boundary condition, target quantities need not be computed since they are prescribed by the setup, so they are chosen corresponding to the prescribed conditions at the inlet.

1. Target values for no-slip boundary conditions

We now need to specify the target values ρ_{tgt}, $\boldsymbol{u}_{\mathrm{tgt}}$, and T_{tgt} for nodes $\boldsymbol{x}_{b,n}$ in the case of no-slip (wall) boundary conditions. The target density ρ_{tgt} corresponds to the density obtained after applying the bounceback rule to the f populations

$$\rho_{\mathrm{tgt}} = \sum_{i\in\overline{D}} f_i^{bb} + \sum_{i\notin\overline{D}} f_i, \tag{109}$$

where the missing populations f_i^{bb} are replaced by the reflected populations as $f_i^{bb} = \tilde{f}_i$ with $\tilde{\boldsymbol{v}}_i = -\boldsymbol{v}_i$. The target velocity $\boldsymbol{u}_{tgt}$ at a given boundary node $\boldsymbol{x}_{b,n}$ is obtained by an interpolation scheme involving the wall velocity $\boldsymbol{u}_{w,i} = \boldsymbol{u}(x_{w,i},t)$ (which usually is 0) at the intersection point $\boldsymbol{x}_{w,i}$ and the velocities $\boldsymbol{u}_{f,i} = \boldsymbol{u}(\boldsymbol{x}_{f,i},t)$ at the adjacent fluid nodes $\boldsymbol{x}_{f,i} = \boldsymbol{x}_b + \boldsymbol{v}_i$ for $i \in \overline{D}$. For an averaged linear interpolation, this yields

$$\boldsymbol{u}_{\mathrm{tgt}} = \frac{1}{n_{\overline{D}}}\sum_{i\in\overline{D}}\frac{(\|\boldsymbol{r}\|_i/\|\boldsymbol{v}\|_i)\boldsymbol{u}_{f,i} + \boldsymbol{u}_{w,i}}{(\|\boldsymbol{r}\|_i/\|\boldsymbol{v}\|_i) + 1}, \tag{110}$$

where $n_{\overline{D}}$ is the number of unknown populations satisfying $\max(\|\boldsymbol{r}\|_i, i \notin \overline{D}) \leqslant \sqrt{2}$ in two dimensions and $\max(\|\boldsymbol{r}\|_i, i \notin \overline{D}) \leqslant \sqrt{3}$ in three dimensions. Similarly, the same procedure is applied to the temperature:

$$T_{\text{tgt}} = \frac{1}{n_{\overline{D}}} \sum_{i \in \overline{D}} \frac{(\|\boldsymbol{r}\|_i/\|\boldsymbol{v}\|_i) T_{f,i} + T_{w,i}}{(\|\boldsymbol{r}\|_i/\|\boldsymbol{v}\|_i) + 1}. \tag{111}$$

The derivatives for a generic field Φ are evaluated with a semi-second-order scheme for the unstructured grid,

$$\frac{\partial \Phi}{\partial x} = \frac{\Phi_{j+1} - \Phi_w}{1 + \|\boldsymbol{r}\|_i} \tag{112}$$

or

$$\frac{\partial \Phi}{\partial x} = \frac{\Phi_w - \Phi_{j-1}}{1 + \|\boldsymbol{r}\|_i}, \tag{113}$$

depending on the position of the wall with respect to the boundary node, where Φ_w is the quantity Φ imposed at the wall (for example, $\boldsymbol{u}$ or T).

2. *Target values for free-slip and adiabatic wall boundary conditions*

Target conditions for free-slip and adiabatic wall boundary conditions can be constructed by starting from the no-flux condition for density and temperature

$$\left.\frac{\partial \rho}{\partial n}\right|_{\partial \Omega} = 0, \tag{114}$$

$$\left.\frac{\partial T}{\partial n}\right|_{\partial \Omega} = 0, \tag{115}$$

where n is the coordinate normal to the boundary surface $\partial\Omega$, as depicted in Fig. 2. For the velocity field, the same condition is imposed for the component of velocity normal to the boundary surface $\partial\Omega$, $\boldsymbol{u}_\perp$:

$$\left.\frac{\partial \boldsymbol{u}_\perp}{\partial n}\right|_{\partial \Omega} = 0. \tag{116}$$

On the other side, the tangent component of velocity $\boldsymbol{u}_\parallel$ is the projection on the surface $\partial\Omega$ of the velocity field $\boldsymbol{u}(\boldsymbol{x}_b)$ at the boundary node:

$$\boldsymbol{u}_\parallel = \boldsymbol{u} - (\boldsymbol{u} \cdot \boldsymbol{n})\boldsymbol{n}, \tag{117}$$

where $\boldsymbol{n}$ is the vector normal with respect to surface $\partial\Omega$. In order to satisfy the no-flux conditions, the values of density, temperature, and velocity are evaluated in the normal direction, by bilinear interpolation, as depicted in Fig. 2. Given the normal direction and then its end point N considering a constant distance from A of $\|\boldsymbol{n}\| = \sqrt{2}$ in 2D or $\|\boldsymbol{n}\| = \sqrt{3}$ in 3D, we identify the neighbors points A, B, C, and D. Next we perform bilinear interpolation (in 2D), for a given field Φ, according to

$$\begin{aligned}\Phi_N = {} & [(D_x - A_x)(B_y - A_y)]^{-1} \\ & \times [\Phi_A(D_x - N_x)(B_y - N_y)\Phi_B(D_x - N_x)(N_y - A_y) \\ & \times \Phi_C(N_x - A_x)(N_y - A_y)\Phi_D(N_x - A_x)(B_y - N_y)].\end{aligned} \tag{118}$$

Here Φ_N is the field to be found at point N and Φ_A, Φ_B, Φ_C, and Φ_D are the known fields at respective points, where A_x, A_y, etc., are the x and y coordinates, respectively, for point A and the same for the other points. A similar procedure for fields at point N, Φ_N, can be performed in three dimensions by trilinear interpolation.

Once Φ_N is found, we assume a first-order approximation for the derivative in the direction of the normal:

$$\frac{\partial \Phi}{\partial n} \simeq \frac{\Phi_N - \Phi_A}{\|N - A\|} = 0. \tag{119}$$

This allows us to approximate the values of the fields at node A:

$$\Phi_A = \Phi_N, \tag{120}$$

which correspond to the target values $\Phi_{\text{tgt}} = \Phi_A$.

III. NUMERICAL VALIDATION

In the following, various numerical simulations are performed in order to validate the model and the boundary conditions described previously. We start by presenting the simulation of the two-dimensional supersonic flow around a diamond-shaped airfoil, for which analytical solutions are available. Next, the two-dimensional inviscid transonic flow around the NACA0012 airfoil is presented for two different angles of attack. In a second part, the results for the viscous transonic flow around the NACA0012 airfoil are exposed. We continue presenting simulations results of the Schardin problem and we conclude with the three-dimensional simulation of the inviscid supersonic flow field around a double cone geometry.

A. Supersonic inviscid diamond airfoil

We start here by presenting, in Fig. 3, the Mach-number distribution around a diamond-shaped airfoil, where free-slip boundary conditions are imposed. The far-field flow is characterized by Mach number $\text{Ma} = 1.5$ and a Reynolds number of $\text{Re} = 3 \times 10^6$, and the angle of attack of the airfoil is set to $\mathcal{A} = 3^\circ$. Typical oblique shocks are formed starting from the leading and trailing edges, while expansions waves are formed at the rear edges of the airfoil.

The setup was simulated with three different chord lengths $C = 100$, 500, and 1000 and is compared with the analytical expression [45] for shocks angles and Mach and pressure

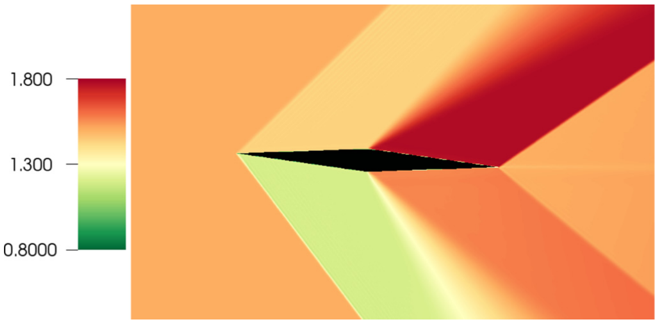

FIG. 3. Mach-number distribution around a diamond-shaped airfoil immersed in a supersonic flow field at $\text{Ma} = 1.5$ and $\text{Re} = 3 \times 10^6$ based on chord length and inflow speed.

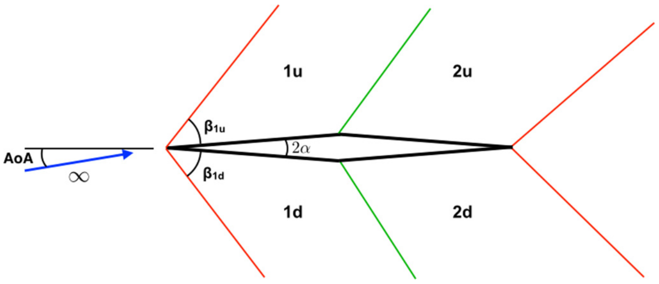

FIG. 4. Scheme of the various zones and angles compared with analytical solutions.

distributions around the airfoil. In Fig. 4 we show the various zones that are compared, together with the corresponding angle definitions.

The angles of the oblique shocks with respect to the surface of the airfoil depend on the upstream Mach number Ma_∞, the angle of attack $\mathcal{A}$, and the angle of the solid geometry 2α and are given by the nonlinear equations

$$\tan(\alpha - \mathcal{A}) = 2\cot\beta_{1u}\frac{\mathrm{Ma}_\infty^2 \sin^2\beta_{1u} - 1}{\mathrm{Ma}_\infty^2(\gamma + \cos 2\beta_{1u}) + 2}, \tag{121}$$

$$\tan(\alpha + \mathcal{A}) = 2\cot\beta_{1d}\frac{\mathrm{Ma}_\infty^2 \sin^2\beta_{1d} - 1}{\mathrm{Ma}_\infty^2(\gamma + \cos 2\beta_{1d}) + 2} \tag{122}$$

for the upper and lower oblique shocks, respectively. Once the angles of the shock are found, it is possible to express the pressure and the Mach number after the oblique shocks:

$$\frac{p_{1u/d}}{p_\infty} = 1 + \frac{2\gamma}{\gamma + 1}\left(\mathrm{Ma}_\infty^2 \sin^2\beta_{1u/d} - 1\right), \tag{123}$$

$$\mathrm{Ma}_{1u} = \frac{1}{\sin^2(\beta_{1u} - \alpha + \mathcal{A})}\frac{\left(1 + \frac{\gamma+1}{2}\mathrm{Ma}_\infty^2 \sin^2\beta_{1u}\right)}{\gamma \mathrm{Ma}_\infty^2 \sin^2\beta_{1u} - \frac{\gamma-1}{2}}, \tag{124}$$

$$\mathrm{Ma}_{1d} = \frac{1}{\sin^2(\beta_{1d} - \alpha - \mathcal{A})}\frac{1 + \frac{\gamma+1}{2}\mathrm{Ma}_\infty^2 \sin^2\beta_{1d}}{\gamma \mathrm{Ma}_\infty^2 \sin^2\beta_{1d} - \frac{\gamma-1}{2}}. \tag{125}$$

In order to find the postexpansion-fan distributions ($2u$ and $2d$), one needs first to evaluate the Prandtl-Meyer function $\nu(\mathrm{Ma})$ for the pre-expansion Mach number

$$\nu(\mathrm{Ma}_{1u/d}) = \sqrt{\frac{\gamma+1}{\gamma-1}}\arctan\sqrt{\frac{\gamma-1}{\gamma+1}\left(\mathrm{Ma}_{1u/d}^2 - 1\right)} - \arctan\sqrt{\mathrm{Ma}_{1u/d}^2 - 1}. \tag{126}$$

Next, the Mach number after the expansion can be evaluated by solving the same equation for the Mach number $\mathrm{Ma}_{2u/d}$, but for a modified Prandtl-Meyer value

$$\nu(\mathrm{Ma}_{1u/d}) + 2\alpha = \sqrt{\frac{\gamma+1}{\gamma-1}}\arctan\sqrt{\frac{\gamma-1}{\gamma+1}\left(\mathrm{Ma}_{2u/d}^2 - 1\right)} - \arctan\sqrt{\mathrm{Ma}_{2u/d}^2 - 1}. \tag{127}$$

Pressure is derived by the pressure upstream of the expansion fan and the Mach number upstream and downstream of the expansion fan:

$$\frac{p_{2u/d}}{p_{1u/d}} = \left(\frac{1 + \frac{\gamma-1}{2}\mathrm{Ma}_{1u/d}^2}{1 + \frac{\gamma-1}{2}\mathrm{Ma}_{2u/d}^2}\right)^{\gamma/(\gamma-1)}. \tag{128}$$

In Table I we report the errors on the two angles β_{1u} and β_{1d} with the three different chord lengths, while in Tables II and III we report the errors on the pressure normalized by pressure at infinity and of Mach number. The reported errors show that the method is sufficiently accurate already with a small Cartesian grid of $C = 100$ for the discretization of the chord of the airfoil. This demonstrates a good predictive capability of the model.

TABLE I. Errors ϵ of the computed oblique shock angles with three different chord resolutions: $C = 100$, 500, and 1000.

	Analytical	ϵ_{100} (%)	ϵ_{500} (%)	ϵ_{1000} (%)
β_{1u}	44.064	2.957	0.467	0.376
β_{1d}	52.572	1.506	0.357	0.205

TABLE II. Errors ϵ of the computed Mach-number distribution around the airfoil and for a chord length of $C = 100$.

	Ma_{1u}	Ma_{1d}	Ma_{2u}	Ma_{2d}
Analysis	1.4316	1.2079	1.7716	1.5626
ϵ_{100} (%)	0.069	1.135	0.206	0.163

B. Transonic inviscid NACA0012 airfoil

In this section we present two simulations in which the transonic flow field around a NACA0012 airfoil is considered. Two different situations were performed: the first with an angle of attack of the airfoil of $\mathcal{A} = 0°$ and a Mach number of $\mathrm{Ma} = 0.82$ and the other with an angle of attack of $\mathcal{A} = 2°$ and a Mach number of $\mathrm{Ma} = 0.75$. For both cases the Reynolds number was set to $\mathrm{Re} = 10^6$, the cord was resolved with $C = 200$ points, and the free-slip boundary conditions were used.

In Fig. 5 the distribution of Mach number around the airfoil for the case with an angle of attack $\mathcal{A} = 0°$, on the left, and for the case with $\mathcal{A} = 2°$, on the right, is represented.

The plot shows the typical shock wave formation for both cases: on both sides of the airfoil for $\mathrm{Ma}_\infty = 0.82$ and $\mathcal{A} = 0°$ and on the upper surface for the case $\mathrm{Ma}_\infty = 0.75$ and $\mathcal{A} = 2°$. This is due to the progressively increasing velocity on the airfoil surface, which gradually becomes supersonic. The pressure distribution for both cases has been compared with experimental measurements, the results of Euler equations solver, and potential equation solver and is shown in Fig. 6.

TABLE III. Errors ϵ of the computed pressure distribution around the airfoil and for a chord length of $C = 100$.

	p_{1u}/p_∞	p_{1d}/p_∞	p_{2u}/p_∞	p_{2d}/p_∞
Analytical	1.1030	1.4887	0.6671	0.9069
ϵ_{100} (%)	0.706	1.404	0.036	0.021

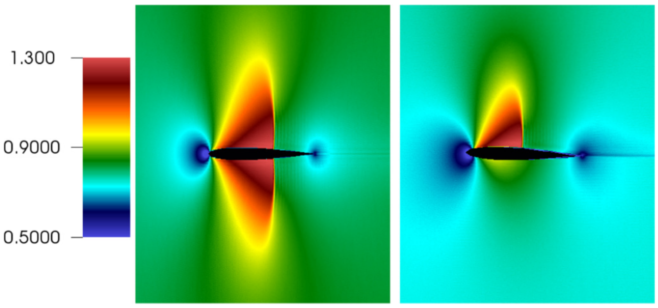

FIG. 5. Distribution of Mach number around the NACA0012 airfoil with $\mathrm{Ma}_\infty = 0.82$ and $\mathcal{A} = 0^\circ$ on the left and $\mathrm{Ma}_\infty = 0.75$ and $\mathcal{A} = 2^\circ$ on the right.

The ELBM solver compares very well with the Euler equations solver, while the shock is more steep if compared to the experimental measurement. This is due to the fact that in the present simulation free-slip boundary conditions were employed, while in the experiment the boundary layer plays a fundamental role in shaping the shock near the wall, diffusing the pressure. The preshock and postshock conditions are however captured correctly. Comparison of the ELBM

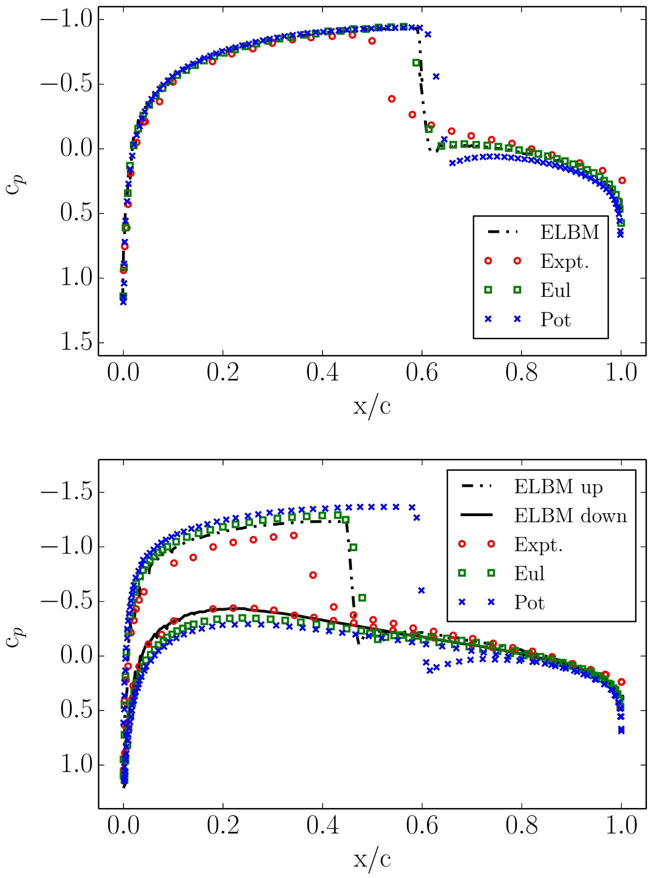

FIG. 6. Pressure coefficient comparison for the transonic flow field around a NACA0012 airfoil for two different Mach numbers and angles of attack, at Reynolds number $\mathrm{Re} = 10^6$: $\mathrm{Ma}_\infty = 0.82$ and $\mathcal{A} = 0^\circ$ (top) $\mathrm{Ma}_\infty = 0.75$ and $\mathcal{A} = 2^\circ$ (bottom). Compared are the ELBM with experimental measurements [46], the Euler solver [47], and the transonic potential equation solver.

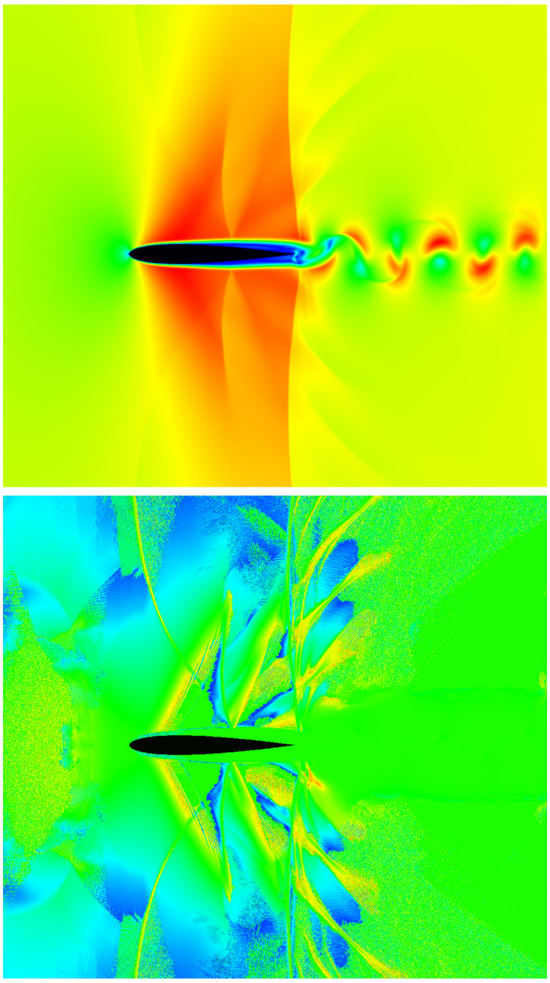

FIG. 7. Mach-number (top) and entropic estimate (bottom) distributions around the NACA0012 airfoil with $\mathrm{Ma}_\infty = 0.85$, $\mathrm{Re} = 10\,000$, and $\mathcal{A} = 0^\circ$.

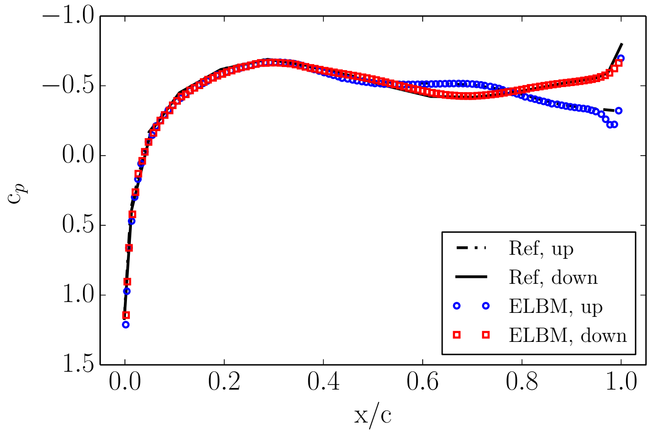

FIG. 8. Pressure coefficient comparison for the viscous transonic flow field around a NACA0012 airfoil with $\mathrm{Ma}_\infty = 0.85$, $\mathrm{Re} = 10\,000$, and $\mathcal{A} = 0^\circ$. Compared are the ELBM and the simulations of [48].

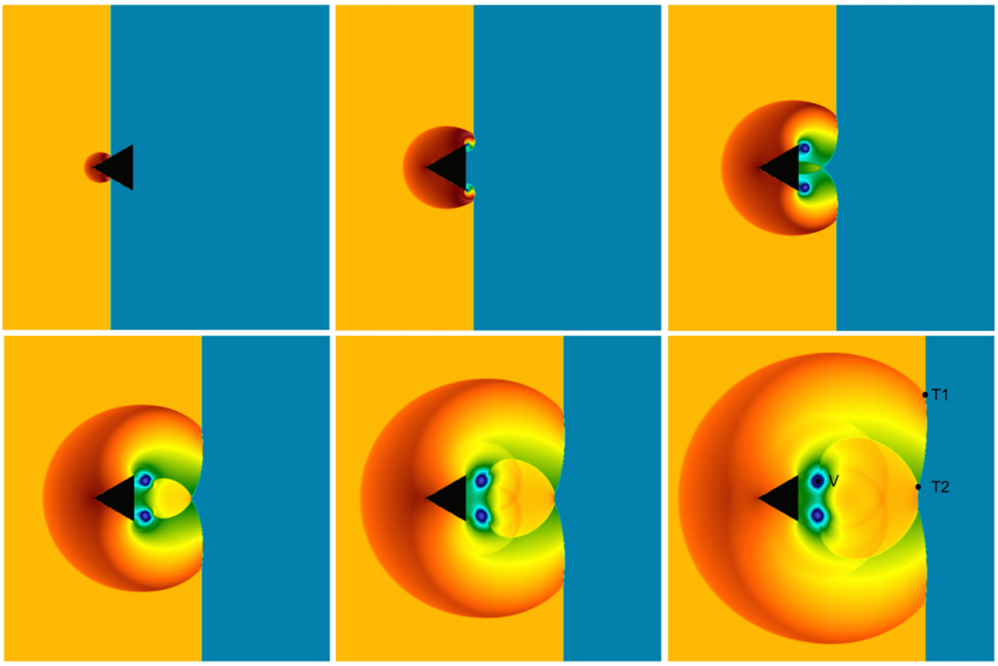

FIG. 9. Evolution of the pressure for the Schardin's problem.

result with the potential solver solution is also provided and it can be noted that both have similar behavior, apart from the fact that the ELBM solver computes the postshock pressure correctly, while the potential solver does not.

For the case with an angle of attack $\mathcal{A} = 2^\circ$, the pressure coefficient on the nonshocked (lower) surface and computed with the ELBM solver compares perfectly with the measurements, while the Euler and potential solvers are slightly incorrect. When the upper shocked surface is analyzed, one can see that the ELBM solution is close to the Euler solution. The deviation from the experiments is due to the reason explained for the case with zero angle of attack and gets amplified when the angle of attack is increased.

C. Viscous transonic NACA0012 airfoil

We proceed by including viscous and boundary layer effects by imposing no-slip and adiabatic boundary condition on the surface of the airfoil. The freestream Mach number was set to $\mathrm{Ma}_\infty = 0.85$, the Reynolds number to $\mathrm{Re} = 10^4$, and the angle of attack to $\mathcal{A} = 0^\circ$. In order to capture the boundary layer correctly, the chord was resolved with $C = 800$ points. Figure 7 shows the distribution of Mach number over the airfoil.

In this configuration, a complex flow field forms on the airfoil surface and downstream: Due to the shear developing from the boundary layer, vortex shedding is initiated downstream the airfoil, with sound waves departing from it and accumulating at the shock front developed above (or below for the lower airfoil surface) the boundary layer. Further upstream another shock forms: Both shocks travel downstream and upstream unsteadily influenced by the vortex shedding.

We plot in Fig. 7 the distribution of the entropic estimate α. One can notice how it follows the flow field patterns (compared to the Mach-number distribution), in particular in the location of the shocks and of the waves emitted by the downstream vortex shedding, helping to stabilize the flow field. In fact, if the entropic estimate was set constant to $\alpha = 2$ (LBGK model), the simulation would become unstable. In order to compare quantitatively the solution obtained with the ELBM, we plot in Fig. 8 the pressure coefficient distribution on the airfoil surface at normalized time $t = 13.8$.

The comparison with the simulations of [48] shows once again the excellent results obtained with ELBM.

D. Schardin's problem

The last two-dimensional validation is conducted by simulating the so-called Schardin problem. In this setup a planar shock wave impinges on a triangular wedge, reflecting and refracting, thus creating complex shock-shock and shock-vortex

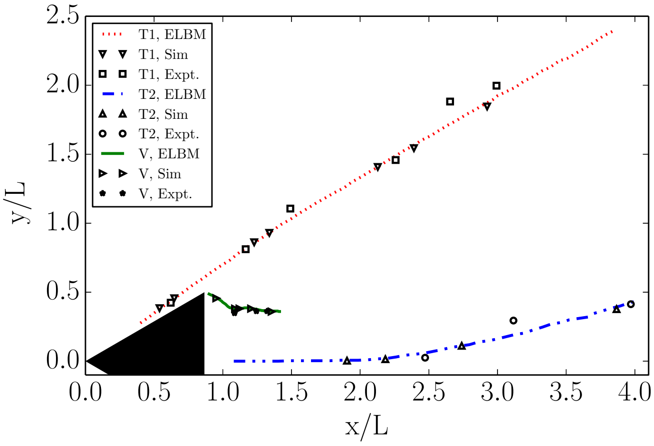

FIG. 10. Evolution of the position of the triple point $T1$, the triple point $T2$, and the vortex V.

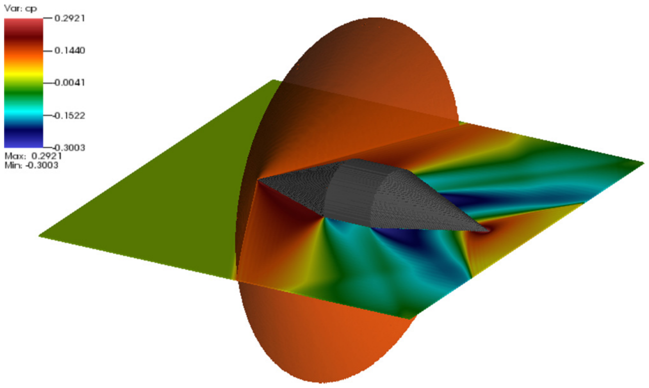

FIG. 11. Slice of the pressure coefficient distribution together with isosurface of density in order to visualize the conical shock wave forming in front of the double cone.

interactions [49,50]. A typical evolution of the flow field for such a problem is shown in Fig. 9 by plotting the pressure distribution for a shock wave traveling at $\mathrm{Ma} = 1.34$ and $\mathrm{Re} = 2000$ based on the wedge length, resolved with $L = 300$ points.

In Fig. 10 the evolutions of the position of the triple point $T1$, the triple point $T2$, and the vortex center V are represented.

E. Supersonic inviscid double cone

Finally we show the results obtained by the three-dimensional simulation of the supersonic flow field around a double cone geometry. The Mach number was set to $\mathrm{Ma}_\infty = 1.3$ and the Reynolds number to $\mathrm{Re} = 10^6$ with zero angle of attack. Free-slip boundary conditions were imposed on the cone surface in order to compare with analytical computations based on inviscid equations. In Fig. 11 we provide an overview of the flow field around the double cone: The slice shows the distribution of pressure coefficient while the orange isosurface of density depicts the conical shock forming in front of the cones.

In order to validate the simulation, we compare in Table IV the angle of the cone formed by the axisymmetric oblique shock, the mean pressure coefficient, and the mean Mach number on the first cone surface with the analytical computations of [51].

Also for the three-dimensional case the comparison is satisfactory, in particular considering the low resolution employed for the simulation.

TABLE IV. Errors with respect to analytical computations [51] of the semiangle of the conical shock θ_s and the mean Mach number on the surface of the first cone Ma_w and on the mean pressure coefficient on the surface of the first cone c_{p_w}. The first cone is resolved with a length of $C = 150$ lattice points.

	θ_s	Ma_w	c_{p_w}
Analytical	58.0°	0.970	0.219
ELBM	58.7°	0.959	0.220
ϵ (%)	1.2	1.1	0.6

IV. CONCLUSION

We presented an extension of the LBM that allows, with one single algorithm, one to simulate a broad range of applications ranging from low Mach number and thermal flows to transonic and supersonic flow regimes, also in the presence of arbitrarily complex obstacles. This is in sharp contrast to conventional solvers, which require identification of different flow regimes and employing the appropriate numerical approach for it.

The model is based on three key elements: higher-order entropy supporting lattices, entropic accurate equilibrium, and entropic time stepping, thus retaining the simplicity of the isothermal LBM. Moreover, detailed boundary conditions were presented in order to simulate the presence of solid walls. These boundaries are validated through a number of standard benchmarks in two and three dimensions.

The simplicity and robustness of the present approach are highlighted by the fact that the construction (adherence to the second law of thermodynamics) and boundary conditions presented here are independent of the choice of the lattice (standard and multispeed lattices) and simulation dimensions. Also, in contrast to the state of the art flow solvers, all ELBM simulations are performed using Cartesian meshes without any grid refinement, turbulence model, tuning parameters, or tracking of the shock front. This, when viewed in combination with the simplicity of the LB methods, could make the ELBM a competitive and viable option for compressible flow simulations.

ACKNOWLEDGMENTS

This work was supported by European Research Council Advanced Grant No. 291094-ELBM. Computational resources from the Swiss National Super Computing Center CSCS were provided under the Grants No. s492 and No. s630. Useful discussion with F. Bösch and B. Dorschner are gratefully acknowledged.

---

[1] S. Pirozzoli, Annu. Rev. Fluid Mech. **43**, 163 (2011).
[2] S. Succi, *The Lattice-Boltzmann Equation* (Oxford University Press, Oxford, 2001).
[3] S. Succi, Europhys. Lett. **109**, 50001 (2015).
[4] P. J. Dellar, Phys. Rev. E **64**, 031203 (2001).
[5] X. Nie, X. Shan, and H. Chen, Europhys. Lett. **81**, 34005 (2008).
[6] D. d'Humières, Philos. Trans. R. Soc. London A **360**, 437 (2002).
[7] H. Xu and P. Sagaut, J. Comput. Phys. **245**, 14 (2013).
[8] I. V. Karlin, F. Bösch, and S. S. Chikatamarla, Phys. Rev. E **90**, 031302 (2014).

[9] I. V. Karlin, A. N. Gorban, S. Succi, and V. Boffi, Phys. Rev. Lett. **81**, 6 (1998).

[10] S. Ansumali and I. V. Karlin, Phys. Rev. E **65**, 056312 (2002).

[11] B. M. Boghosian, J. Yepez, P. V. Coveney, and A. Wager, Proc. R. Soc. London A **457**, 717 (2001).

[12] S. Ansumali, I. Karlin, and H. Öttinger, Europhys. Lett. **63**, 798 (2003).

[13] J. Latt and B. Chopard, Math. Comput. Simul. **72**, 165 (2006).

[14] R. Zhang, X. Shan, and H. Chen, Phys. Rev. E **74**, 046703 (2006).

[15] S. S. Chikatamarla and I. V. Karlin, Phys. Rev. Lett. **97**, 190601 (2006).

[16] S. S. Chikatamarla and I. V. Karlin, Phys. Rev. E **79**, 046701 (2009).

[17] S. Chikatamarla, C. Frouzakis, I. Karlin, A. Tomboulides, and K. Boulouchos, J. Fluid Mech. **656**, 298 (2010).

[18] N. Frapolli, S. S. Chikatamarla, and I. V. Karlin, Phys. Rev. E **90**, 043306 (2014).

[19] N. I. Prasianakis and I. V. Karlin, Phys. Rev. E **76**, 016702 (2007).

[20] X. He, S. Chen, and G. D. Doolen, J. Comput. Phys. **146**, 282 (1998).

[21] Z. Guo, C. Zheng, B. Shi, and T. S. Zhao, Phys. Rev. E **75**, 036704 (2007).

[22] I. V. Karlin, D. Sichau, and S. S. Chikatamarla, Phys. Rev. E **88**, 063310 (2013).

[23] F. J. Alexander, S. Chen, and J. D. Sterling, Phys. Rev. E **47**, R2249 (1993).

[24] G. R. McNamara, A. L. Garcia, and B. J. Alder, J. Stat. Phys. **81**, 395 (1995).

[25] X. Shan and X. He, Phys. Rev. Lett. **80**, 65 (1998).

[26] X. Shan, X.-F. Yuan, and H. Chen, J. Fluid Mech. **550**, 413 (2006).

[27] P. C. Philippi, L. A. Hegele, Jr., L. O. E. dos Santos, and R. Surmas, Phys. Rev. E **73**, 056702 (2006).

[28] R. Surmas, C. P. Ortiz, and P. Philippi, Eur. Phys. J. Spec. Top. **171**, 81 (2009).

[29] N. Frapolli, S. S. Chikatamarla, and I. V. Karlin, Phys. Rev. E **92**, 061301(R) (2015).

[30] I. Karlin and P. Asinari, Physica A **389**, 1530 (2010).

[31] I. V. Karlin, S. S. Chikatamarla, and S. Ansumali, Commun. Comput. Phys. **2**, 196 (2007).

[32] X. He and L.-S. Luo, Phys. Rev. E **56**, 6811 (1997).

[33] S. S. Chikatamarla, S. Ansumali, and I. V. Karlin, Phys. Rev. Lett. **97**, 010201 (2006).

[34] R. A. Brownlee, A. N. Gorban, and J. Levesley, Phys. Rev. E **75**, 036711 (2007).

[35] I. Karlin, A. Ferrante, and H. Öttinger, Europhys. Lett. **47**, 182 (1999).

[36] S. Ansumali, S. Arcidiacono, S. Chikatamarla, N. Prasianakis, A. Gorban, and I. Karlin, Eur. Phys. J. B **56**, 135 (2007).

[37] X. Shan and H. Chen, Int. J. Mod. Phys. C **18**, 635 (2007).

[38] E. Shakhov, Fluid Dyn. **3**, 95 (1968).

[39] T. Kataoka and M. Tsutahara, Phys. Rev. E **69**, 035701 (2004).

[40] F. Chen, A. Xu, G. Zhang, Y. Li, and S. Succi, Europhys. Lett. **90**, 54003 (2010).

[41] V. Rykov, Fluid Dyn. **10**, 959 (1975).

[42] X. Nie, X. Shan, and H. Chen, Phys. Rev. E **77**, 035701 (2008).

[43] A. Mazloomi M, S. S. Chikatamarla, and I. V. Karlin, Phys. Rev. Lett. **114**, 174502 (2015).

[44] B. Dorschner, S. Chikatamarla, F. Bösch, and I. Karlin, J. Comput. Phys. **295**, 340 (2015).

[45] H. W. Liepmann and A. Roshko, *Elements of Gasdynamics* (Courier, New York, 1957).

[46] C. L. Ladson, A. S. Hill, and W. G. Johnson, Jr., Pressure Distributions from High Reynolds Number Transonic Tests of an NACA 0012 Airfoil in the Langley 0.3-Meter Transonic Cryogenic Tunnel, Technical Report (NASA Technical Memorandum 100526, 1987).

[47] C. Hirsch, *Numerical Computation of Internal and External Flows: The Fundamentals of Computational Fluid Dynamics* (Butterworth-Heinemann, Oxford, 2007), Vol. 1.

[48] N. Satofuka, K. Morinishi, and Y. Nishida, in *Numerical Simulation of Compressible Navier-Stokes Flows* (Springer, Berlin, 1987), pp. 201–218.

[49] S.-M. Chang and K.-S. Chang, Shock Waves **10**, 333 (2000).

[50] P. Halder, S. De, K. Sinhamahapatra, and N. Singh, Shock Waves **23**, 495 (2013).

[51] G. Taylor and J. Maccoll, Proc. R. Soc. London A **139**, 278 (1933).